Turner, Paul and Liu, Tao and Zeng, Xuesen (2016) Collapse of 3D orthogonal woven carbon fibre composites under in-plane tension/compression and out-of-plane bending composite structures. Composite Structures . ISSN 1879-1085

Collapse of 3D Orthogonal Woven Carbon Fibre Composites Under In-plane Tension/Compression and Out-of-plane Bending

P.Turner[a,b,c], T.Liu[a,b,c]* and X.Zeng[b]

[a]*Centre for Structural Engineering and Informatics*
[b]*Composites Research Group,*
[c]*Department of Civil Engineering*

Faculty of Engineering, The University of Nottingham,
University Park, Nottingham, NG7 2RD, U.K.

Corresponding author :Tao.Liu@nottingham.ac.uk

Tel: + 44 (0)1159 5 84059, Fax: +44 (0) 115 74 84059

Abstract

An experimental and numerical investigation was undertaken to characterise the collapse of 3D orthogonal woven carbon fibre composites during the load cases of in-plane tension, in-plane compression and out-of-plane bending. Two different fibre architectures, varying only by the density of through-thickness reinforcement, were investigated. Cantilever beam tests were carried out to isolate two distinct collapse mechanisms, i.e. bending governed and shear governed deformation. A qualitative comparison was made with a similar UD-laminate material. 3D woven composites exhibited significantly reduced delamination. An investigation into the efficacy of an embedded element modelling strategy for in-plane tension, in-plane compression and out-of-plane bending load cases was undertaken. The predictions were generally in good agreement with the experimental measurements for the in-plane and out-of-plane loading.

Key words

1. Introduction

Three-dimensional woven composites contain woven textile reinforcement with yarns orientated along the x-axis, the y-axis and the z-axis. They have a distinct advantage over two-dimensional fibre reinforced composites due to their enhanced inter-laminar and flexure properties. The in-plane response has been investigated at depth within the literature. Prominent examples include the tensile properties [1-8], and the compressive properties [1, 9, 10]. However, the principle reasoning behind the addition of the through-thickness reinforcement is to improve the inter-laminar and out-of-plane bending properties of the composite.

The double cantilever beam (DCB) is an effective methodology for determining the Mode I inter-laminar fracture toughness of fibre reinforced composites. The DCB studies on 3D woven carbon/epoxy materials recorded increases in Mode I inter-laminar fracture toughness up to 15 times than that of a 2D carbon/epoxy laminate [11] and greatly increased strain-energy release rates of 3D composites in comparison to 2D composites [12]. This increase was attributed to crack-bridging and crack-diverting. Mode II inter-laminar fracture toughness is commonly measured via the end loaded split (ELS) [13-15] and three [16, 17] and four-point [15, 18] end notch flexure (3ENF and 4ENF) testing methodologies. ELF and 4ENF experiments undertaken upon 3D woven composites have suggested that there is a relatively greater role for the matrix in Mode II crack propagation in comparison to Mode I crack propagation, and therefore increases of binder density present a relatively lower increase in Mode II toughness. [15].

The flexural properties of fibre reinforced composite materials are commonly investigated in two standard tests: three-point bending tests [1, 19-24], and four-point bending tests [23-26]. During three-point bending tests, stress concentrations have been reported to cause early-

onset microcracking of the matrix and subsequent localised non-linearity [20], potentially leading to catastrophic failure of the beam [27]. The load concentration of the three-point bending test leads to a combination of bending with shear stresses [27], causing difficulty in the isolation of either one. Also, for composites with high levels of orthotropy, both a flexural and a twisting curvature is introduced throughout the beam length, which adds to the complication during three-point bending tests [28]. The four-point bending test is an attractive alternative as it induces pure bending stresses within the beam. However, due to rotation at loading rollers during four-point bending, the load span increases during the test, overestimations of flexural modulus are common if corrections are not made [25].

Gerlach et al. [21] investigated the out-of-plane properties of a through-the-thickness angle interlock 3D woven carbon composite material with a three-point bending test and plate bending test. The results indicated that binder density influences delamination length, however, the tests were highly dependent on support conditions and loading roller geometry. Zhang et al.[29] investigated a layer-to-layer orthogonal interlocked textile composite under three point bending, employing DIC to capture local increases in strain and microcracking. However, due to the localised damage initiation experienced in textile composites, interpretation of a catastrophic failure event during a three-point bending test can be complicated by the asymmetric nature of the failure; damage could occur in either or both of the two arms of the beam. Damage could also occur under the loading roller, complicating damage progression analysis [30]. Liu et al.[31] applied a cantilever beam test procedure to Dyneema material. This method proved useful in simplifying the analysis of beam collapse under bending. The research presented here adopts the cantilever beam test in order to activate two distinct collapse mechanisms for 3D woven carbon/epoxy composite materials. It then provides a clear analysis of the progression of the collapse event throughout the test

coupon. This is supplemented with further investigation into the two collapse modes via the use of the Finite Element (FE) method.

A common methodology in the numerical prediction of the stiffness and strength of woven composites is the FE analysis at a unit cell level [32-38]. Nagai et al. [32] used micro-mechanical FE analyses at the unit cell level in order to present a structural analysis model. The unit cell, composing of fibre (beam) elements and matrix (beam and rod) elements, was imparted with an enforced displacement in order to extract the non-linear properties. These properties were then translated to homogenous solids for use in the structural analysis for tensile, compressive and shear mechanical behaviour up to failure. The structural analysis model was used exclusively for undulated fibre composites, and was validated through experiments. Huang et al. [37] conducted a 3D multi-unit cell FE simulation in order to investigate the compressive strength and failure mechanisms of woven textile composites. They found that 16 unit cells gave good agreement to experimental results [37]. Kink band formation was determined as the main compressive strength limit factor [38]. Modelling at the representative volume element (RVE) level is an alternative to unit cell based modelling methodologies [39-41]. However, modelling at the RVE level has been known to exhibit reduced accuracy due to the lack of geometric detailing [39].

The Binary Model [42-44] attempts to move away any assumptions of periodicity within the material. It was used for simulating relatively large, three-dimensional models of textile composites, whilst paying particular attention to the induced stochastic flaws introduced into the material during manufacturing. The model uses beam elements to represent fibre tows, which are then embedded within a solid effective medium that represents the matrix. The Binary Model can incorporate non-linearity in both the reinforcing tow and matrix easily, and was shown to reproduce well the qualitative features of stress-strain curves for uni-axial tests

4

on a 3D woven angle interlock material. Readers are referred to [45] for a more comprehensive overview of modelling strategies for 3D woven composite materials.

The experimental component of this paper utilises uni-axial tension and compression tests and a cantilever beam bending test. By varying the length of beam during the cantilever beam test, two distinct collapse mechanisms experienced by orthogonal 3D woven composites during out-of-plane loading were isolated. Two different densities of orthogonal through-the-thickness reinforcement were tested. The numerical method is developed as a viable finite element strategy for modelling full scale 3D woven composites test coupons. The FE model aims to be computationally efficient, utilising embedded shell elements representing the reinforcement tows within solid matrix elements.

2. 3D woven composite material and in-plane tension/compression coupon tests

This study used 3D orthogonal woven carbon fibre reinforcements with two through-the-thickness (TTT) binder densities. The two different fibre architectures are shown in Figure 1. The "Full TTT" material has a binder-to-warp-stack ratio of 1:1 (i.e. each binder tow being separated by one vertical stack of warp tows), while the "Half TTT" material has a binder-to-warp-stack ratio of 1:2. Throughout this paper, the warp tow direction is referred to as the x-direction, the weft tow direction is referred to as the y-direction and the through-the-thickness direction is referred to as the z-direction. Microscopic images of the cured composite cross-sections were used to measure the average values for the dimensions of the fibre architecture. The average dimensions are presented in Figure 1. Both materials contained an alternating stack of 9 weft layers and 8 warp layers giving a total thickness of 3.5 mm for the cured composite. The overall fibre volume fraction was 0.56 for the full TTT composites, and 0.55 for the half TTT composites. The carbon fibre tows were AKSACA A-38 with 6K filaments for warp and weft tows, and 3K filaments for binder tows. Epoxy resin was Gurit Prime

20LV, with the ratio of slow hardener to resin by weight as 26:100. Standard vacuum infusion technique was utilised for the resin injection. Further details of the composite material are presented by Turner et al. [46].

Quasi-static (2mm/min) uniaxial material coupon tests were conducted on the Full TTT 3D woven composites, in order to determine the in-plane mechanical properties under tension and compression. The in-plane tension and compression experimental procedure was identical to that presented by Turner et al. [46], adopting EN ISO 527-4 methodology for tensile testing, and ASTM D3410/B for compression testing. Five repeat measurements were taken for tension and compression tests in warp and weft directions. The tensile and compressive tests in the ±45° orientation were performed in a way that warp and weft tows lay at ±45° to the loading axis.

3. Cantilever beam test protocol

Figure 2(a) presents a sketch of the cantilever beam set-up. Beam specimens of width $w = 20$ mm were cut along both directions (longitudinal warp or weft yarns), from the two different 3D woven composites panels. One end of the beams was clamped into a custom-designed fixture in stainless steel with M6 bolts. This fixture was subsequently bolted onto a steel I-Beam attached to an Instron 5581 test machine with a static 50 kN load cell. The Instron test machine provided a constant displacement rate at 4mm/min for a 10 mm diameter roller in constant contact with the free end of the beams. The diameter of the loading roller was chosen to match current 3-point [47-49] and 4-point [47] flexural test method standards. The roller diameter was deemed large enough to reduce local surface fibre damage caused by contact stresses. Initial testing indicated that the length of the cantilever beam that extended past the roller loading position had no influence on the response of the beams. The front surface of the beams were speckle painted for DIC analysis. Figure 2(b) presents a sketch of

6

the cantilever beam test orientated along the x-direction (warp) showing the fibre reinforcement topology in relation to the beam.

4. Finite element Analysis

A FE modelling strategy, used for the prediction of the in-plane and out-out-plane responses of the orthogonal 3D woven carbon fibre reinforced composite, will now be presented. The primary aims of the numerical calculations presented in the following sections are:

- To examine the efficacy of the embedded element modelling technique employing the constitutive models of Matzenmiller et al. [50] and Hashin [51] for fibre composites.

- To provide in-depth understanding of the experimental results.

4.1   FE model of orthogonal 3D woven composites

A three dimensional (3D) finite element analysis was conducted by using the explicit solver in ABAQUS (Version 6.12). Each individual tow in weft, warp and TTT-directions was modelled with 4-noded doubly curved shell elements (S4 in ABAQUS notation), with five integration points through the thickness. The length of side of each element was 0.25 mm. See Figure 3 for a sketch of the meshed finite element model. The orientation option within ABAQUS was used to assign the local fibre orientations of individual tows. The geometric data for defining the locations and cross sectional areas of the tows or TTT-reinforcement were taken from microscopic images. The fibre architecture varies throughout the structure due to the presence of the binder and randomly orientated stochastic flaws. Therefore, an average was taken in order to recreate the geometry of the specimen in the FE model. The matrix was modelled using quadratic solid elements (C3D8 in ABAQUS notation) of second-order accuracy. The total number of shell and solid elements was 91,000 elements for the short beam model, and 474,000 elements for the long beam model; a numerical study

demonstrated that this mesh density achieved a converged result. Shell elements, representing the reinforcement tows, were embedded within the solid elements, which represents the resin matrix. The translational Degrees of Freedom (DoF) of the nodes in the shell elements are constrained to the interpolated values of the corresponding DoF in the solid elements (host elements).

For cantilever beam simulation, the loading roller was simulated as a discrete rigid body (using R3D4 elements in ABAQUS notation). The roller was moved along the z–direction with a constant displacement. General contact option in ABAQUS was used to model the interaction between the roller and the cantilever beam with a tangential friction coefficient of 0.3. The translational degrees of freedom of the matrix, and the translation and rotational degrees of freedom of the tows were constrained at the clamped end of the beam simulations. This gave a free length of 8 mm for short beam calculations and 40 mm for long beam calculations. Simulations were conducted on 40 mm length long beams, as opposed to the longest beam length tested, in order to reduce calculation time. For the simulation of the in-plane tension and compression tests, the translational degrees of freedom of the edge of the matrix, and the translation and rotational degrees of freedom of the edge of the tows were constrained at one end of the sample, and the other end subjected to a constant displacement along either the x or y-direction. The simulations were conducted in parallel mode (8 CPUs) using the High Performance Computing (HPC) facility at the University of Nottingham.

The constitutive models of Matzenmiller [50] and Hashin [51] for fibre composites were employed to capture the observed collapse modes of tows and TTT-reinforcement. Plane-stress elastic properties were employed for the tow and TTT reinforcement. As the stress state within the elements surpass the Hashin damage initiation criteria damage locus, four scalar damage variables, corresponding the four damage modes, are introduced to represent the

8

effects of the damage modes. Post initiation of damage, the response of the material is

governed by
$$
\begin{Bmatrix} \varepsilon_{11} \\ \varepsilon_{22} \\ \gamma_{12} \end{Bmatrix} = \begin{Bmatrix} 1/[\overline{E}_{11}(1-d_f)] & -\overline{v}_{21}/[\overline{E}_{11}(1-d_f)] & 0 \\ -\overline{v}_{12}/[\overline{E}_{22}(1-d_m)] & 1/[\overline{E}_{22}(1-d_m)] & 0 \\ 0 & 0 & 1/[\overline{G}_{12}(1-d_s)] \end{Bmatrix} \begin{Bmatrix} \sigma_{11} \\ \sigma_{22} \\ \sigma_{12} \end{Bmatrix}
\tag{1}
$$

where
$$
d_f = \begin{cases} d_f^t & \text{if } \sigma_{11} \geq 0 \\ d_f^c & \text{otherwise} \end{cases} \quad \text{and} \quad d_m = \begin{cases} d_m^t & \text{if } \sigma_{22} \geq 0 \\ d_m^c & \text{otherwise} \end{cases}
\tag{2}
$$

Here, d_f^t, d_f^c, d_m^t and d_m^c are the damage variables for fibre damage under tension and

compression, matrix damage under tension and compression, respectively. d_s is the shear

damage variable, defined as

$$
d_s \equiv 1 - (1-d_f^t)(1-d_f^c)(1-d_m^t)(1-d_m^c)
\tag{3}
$$

The shear damage variable is used later in order to visualise the location of damage during

finite element simulations of in-plane uni-axial coupon tests. It is useful as a "resultant"

damage variable combining tension and compression for both longitudinal and transverse

directions. The behaviour of the tow and TTT reinforcement elements post-damage is

governed by a linear softening relationship, as determined by the materials fracture energy. A

characteristic length scale across a finite element, l_e, is included in order to help alleviate

mesh dependency. A more detailed description of the constitutive laws employed within the

finite element modelling in this study is presented in the supplementary data to this paper.

The matrix was treated as a J2-flow theory based elastic-ideally plastic material. A critical

Von Mises effective strain was used for damage initiation. Post damage initiation, a damage

variable, D, was employed for the linear degradation of the elasticity, i.e. $(1-D)E_m$, and for

the linear softening of the yield stress, i.e. $(1-D)\hat{\sigma}_Y^o$. The post damage initiation behaviour of

the material is governed by the matrix fracture energy. The matrix was split into 17 layers

through the thickness, representing each of the 17 individual layers of the fibre reinforcement. A cohesive contact law was used to model the interface between the layers. This simulates the traction-separation behaviour between them and allows the FE model to capture delamination at these locations. It is noted that it was at these locations that delamination occurred during experimental testing. An uncoupled quadratic maximum stress damage initiation criterion was used, and a linear softening law employed post damage initiation with the behaviour governed by the defined fracture energy. The values for the parameters of the cohesive law are presented in the supplementary data to this paper. A detailed description of the constitutive models with the finite element strategy, and of the derivation of the material properties, is presented in the supplementary data to this paper. In short, the majority of the material properties for the fibre reinforcement were calculated from uni-axial tension and compression tests, and the matrix material properties were taken from manufacturer's data and uni-axial coupon tests with the fibre reinforcement orientated at ±45° to the loading axis. The values used for the material properties are also presented in the supplementary data to this paper.

5. Results and discussion

5.1 *Collapse of coupons during in-plane tension and compression loading*

Characteristic tensile and compressive stress-strain curves of the 3D woven carbon composite are presented in Figure 4. The measured Young's Modulus in the tensile tests were 44.3 and 74.6 GPa for warp and weft directions, respectively. The tension and compression tests showed elastic-brittle fracture both in the warp and weft directions. This was governed mainly by fibre reinforcement fracture, as being observed from scanning electron microscopic (SEM) images of the fracture surfaces. Fracture occurred at the location of the TTT-reinforcement for both compression and tension testing of samples orientated along the

10

y-direction (weft). Fracture location was attributed to stress concentrations due to crimping of longitudinal tows at the TTT-reinforcement location. No significant delamination, and no buckling of plies was recorded during these tests. Material tests conducted with fibres orientated at ±45° show a weaker but more ductile response as they are governed by the relatively soft matrix material. This is consistent with the behaviour observed by Gerlach et al. [21] for an orthogonal 3D woven carbon composite material tested with fibres orientated ±45° to loading direction.

For model validation, finite element calculations of in-plane tension and compression test coupons were conducted. Good fidelity between the finite element modelling and experimental measurements was achieved, and the predictions are presented alongside the experimental results in Figure 4. The FE simulation captures the stiffness and peak stress of uniaxial compression/tension tests. The FE model can also provide further insights into the nature of the collapse event within the material. Figure 5(a) presents the predicted contour of in-plane stress along y-direction (weft), σ_{yy}, under y-direction (weft) uniaxial compression testing, immediately prior to failure of the sample. At the positions of the TTT-reinforcement, there is a clear increase in magnitude of σ_{yy}. This is attributed to crimping within the surface weft tows induced by the TTT-reinforcement. The predicted ratio of maximum to minimum stress σ_{yy} in the surface weft tows is approximately 4.0, with the peak stress immediately prior to fracture being identical to that of the longitudinal compressive strength of weft tows, $\overline{X}^C = 1.1$ GPa. This notably high ratio is analogous to the stress concentration factor of 5.5 recorded in notched CFRP samples under compression fatigue loading [52], which is defined as the ratio of local stress to remote stress. To understand the stress distribution through the thickness of the sample, Figure 5(b) shows the contours of σ_{yy}, immediately prior to failure,

11

within the central weft tow stack, as highlighted in Figure 5(a). Again, both top and bottom surface tows have significant stress concentrations owing to crimping induced by the TTT-reinforcement. However, as the crimping has less influence on the geometries of the internal weft tows than those of the surface tows, the stress concentrations in the internal tows are less significant. The staggered binder location at the top and bottom surfaces of the material causes an alternating pattern of increased and reduced local stresses throughout the thickness of the material. This stress variance leads to the "step" shape fracture phenomena. The location of the fracture surface corresponds to the position of maximum longitudinal stress σ_{yy} shown in Figure 5(a) and follows the stress distribution through the thickness shown in Figure 5(b). Figure 5(c) and (d) show the fractured sample obtained by FE simulation and experiment, respectively. The contour in Figure 5(c) shows the damage variable, d_s, within the tows.

For the same sample under tensile testing along y-direction (weft), Figure 6(a) shows the contours of in-plane stress along y-direction (weft), σ_{yy}, within the top surface layer tows, while (b) shows the shear damage variable, d_s, at the fracture surface of the fibre reinforcement immediately after sample fracture. Although the response was governed by the tensile response of the in-plane tows, the shear damage variable was chosen as it allows a convenient visualisation of a combination of the four damage modes. Once fracture initiates within a longitudinal weft tow, it rapidly propagates throughout the material, through the centre of the TTT-reinforcement. Again, the increase in longitudinal stress, σ_{yy}, at the TTT-reinforcement position gives rise to final fracture. In Figure 6(a), the ratio of maximum to minimum stress σ_{yy} in the weft tow is approximately 1.8, with the maximum stress prior to the onset of fracture being 1.72 GPa which is equal to the longitudinal tensile strength of the

12

weft tows, $\overline{X}^T$. The maximum to minimum stress ratio during tensile testing is lower than that of the compressive testing. This is because during the tensile test, the loading acts to "straighten out", the yarns, thus, reducing the effect of crimp. The FE predication is consistent with experimental observation, i.e. the fracture occurred at a TTT-reinforcement position. Figure 6(b) and (c) presented the prediction and observed fracture surface from the experiment. The contour in Figure 6(b) is the shear damage criterion, d_s, with a value of 1 indicated elements which are fully damaged. The numerical calculation correctly predicts the "step" shape fracture surface, located between two neighbouring crimp positions.

5.2   Cantilever beam collapse mechanisms

In order to classify the collapse response of the beams, a set of experiments were conducted with cantilever beams of varying length loaded to failure. Through this, it was possible to identify two distinct collapse mechanisms, and the transition between them. Figure 7(a) presents the force applied by the roller against normalised roller deflection $\overline{\delta} = \delta / L$ along the z-direction for a range of beam lengths. The roller displacement is normalised against the cantilever beam length. Beam collapse is defined as the initial drop-off in resisted load for the shear mechanism, and the drop-off of load resisted after initial period of non-linearity for bending dominated mechanisms. These locations are marked on Figure 7(a). For brevity, only the set of experiments of beams of Full TTT material, with beams orientated along the x-direction (warp) are presented. Beams orientated along the weft direction, and beams of Half TTT material exhibited the same characteristics. The results demonstrate two distinct collapse responses. The short beams, i.e. 7 mm, 8mm, and 10 mm beam lengths, have a linear elastic response up until collapse, and then demonstrate a secondary rise in load resisted before ultimate beam failure. Long beams, i.e. 15 mm, 40 mm and 110 mm, exhibit a softening regime and then an incremental reduction in load resisted until failure. The moment of beam

13

collapse is highlighted on each of the load-deflection curves presented in Figure 7(a). Figure 7(b) presents the collapse load P_c of the beams as a function of beam length L. The two distinct regimes are visible from the data. Simple beam theory was used to curve fit the effective stress within the beam at collapse. It is presented as an approximation in order to demonstrate the transition between the two regimes, i.e. $P_c^b = \sigma_x Wt^2/6L$ for bending dominated long beams and $P_c^s = \tau_{xy} Wt$ for shear dominated short beams. Curve fitting bending dominated beam theory gave the peak stress at collapse of $\sigma_x = 590$ MPa . This value is seen to correspond well to the longitudinal tensile strength along the x-direction (warp) of the composite material, i.e. $\sigma_x = 595$ MPa (presented in Figure 4(a)). Comparison is made to the tensile strength, as tensile crack propagation was the dominant failure mechanism presented by the long cantilever beams. For the shear regime, curve fitting beam theory gave an average shear stress at collapse of $\tau_{xy} = 46$ MPa . The matrix dominated response of tensile coupon tests with fibres orientated at ±45° to the loading axis (Figure 4(a)) predicts the matrix strength at the onset of non-linearity of the test demonstrated to be 80 MPa. Assuming the shear strength to be half of this value, i.e. $\tau_{xy} = 40$ MPa , corresponds acceptably with the collapse response demonstrated during the cantilever beam tests. However, in reality the composite material demonstrates a highly non-linear shear response [53], and therefore this value is only used as a guide. In Figure 7(b), the transition beam length between shear and bending dominated collapse regimes is estimated to be approximately $L \approx 12.5$ mm. For the detailed study, beam lengths 8 mm and 40 mm were selected as representative of shear dominated collapse and bending dominated collapse mechanisms, respectively.

14

5.3   Long cantilever beam bending collapse

As previously demonstrated, the collapse behaviour of the long cantilever beams is governed by bending deformation rather than by shear deformation. Figure 8(a) and (b) show the force imposed by the roller as a function of roller displacement along z-direction for long (40 mm) cantilever beams for Full TTT and Half TTT material orientated along the x-direction (warp) and y-direction (weft), respectively. Also presented is the FE prediction of a long (40 mm) beam collapse event for a Full TTT beam orientated along the x-direction (warp). For both orientations, there was shown to be no significant difference between the two materials tested. To understand the failure mechanism of the long beams, Figure 8(c) shows the full field strain measurement ε_{xx} for normal strain along x-direction (warp) on the front surface of the beam, acquired by the Digital Image Correlation (DIC) technique, for the composite beam with Full TTT reinforcement orientated along the x-direction (warp). The images can be related to the corresponding load – displacement relation shown in Figure 8(a). In the elastic region, up to point A, there are localised increases of tensile strain at the top of the beam. These locations correspond to the positions of TTT reinforcement in the specimen. The load-displacement response became non-linear from point A to Point B, which corresponds to an increase in local compressive strain at the bottom of the beam. Optical microscopic images of the beam post-test, presented in Figure 8(c), reveal the presence of fibre microbuckling of longitudinal tows and crushing of a transverse tow at the clamped edge. Post peak load, at Point C, a tensile crack initiates at the clamped location. Progressive drop-off in load resisted by the beam is attributed to the propagation of the tensile crack. No delamination was observed during either the Full TTT or the Half TTT long beam cantilever tests. The failure mode was identical for both warp and weft direction for both binder densities of the long beam test.

For long cantilever beams, Figure 8(a) shows a comparison between experimental measurement and FE predictions of the force imposed by the roller as a function of roller displacement along z-direction with length of the beam, $L = 40$ mm, and thickness , $t = 3.5$ mm. As the characteristics of the behaviour of the warp and weft orientated beams were the same, i.e. initial linear elastic behaviour followed an a period of non-linearity and progressive reduction in load resisted by the beam, for brevity, only the numerical calculations of the beam oriented along warp direction is presented. The agreement between experimental measurements and FE predictions is reasonably good. Figure 8(d) shows the montage obtained by FE calculations with contour representing strain along x–direction, ε_{xx}. As expected, the long beam failed under bending mechanism, i.e. tensile failure within top tows and compressive failure within bottom tows. At Point A, immediately prior to peak load, there is seen to be an increase of local compressive longitudinal strain at the bottom of the beam at the clamp position. Between Point A and Point B there is a rapid drop-off in load resisted by the beam, caused by an increase of tensile fibre damage of longitudinal warp tows at the top of the beam. This corresponds well to the tensile crack recorded during experimental testing. Tensile fibre damage is the cause of the local increase in tensile longitudinal strain at the top of the beam, seen at Point B. It is proposed that the modification of the linear softening compressive damage evolution law in compression is necessary to fully capture the post damage response of the cantilever beam, i.e. the non-linearity due to kink band formation and tow buckling. In between Point C and D, the FE prediction captures progressive, sudden reductions in load resisted by the beam. The FE model identifies these load reductions to the successive compressive damage of tows located at the clamp. The numerically predicted buckling length of warp tows at the bottom of the beam was approximately 1.5 mm, this coincides to the gap in between TTT-reinforcement positions. Figure 9(a) shows a μ-CT image of the tensile bending crack within the long cantilever beam

post-test. Beam was Full TTT material oriented along the x-direction (warp). The image shows the bending crack following the edges of the TTT reinforcement. The long cantilever beam bending collapse response of a UD-laminate material is presented in the supplementary data to this paper (Figure S.1). In short, the UD-laminate material exhibited extensive delamination throughout the entire length of the beam after initial collapse. This differs from the collapse mechanism demonstrated by the 3D woven composite material.

5.4   Short cantilever beam bending collapse

As previously demonstrated, the collapse behaviour of the short cantilever beams is governed by a shear dominated mechanism. Figure 10(a) and (b) shows the force imposed by the roller as a function of roller displacement along the z-direction for the short cantilever beams with Full and Half TTT 3D woven composites, with beams oriented along x-direction (warp) and y-direction (weft), respectively. The shaded areas represent the range of 3 individual test repeats. For both beam orientations, the density of the TTT reinforcement has small effect on the load-displacement relationship of the short cantilever beams. The Full TTT beams are shown to exhibit a marginally higher secondary increase in load resisted after the initial collapse. DIC images showing the shear strain, γ_{xz} field are shown in Figure 10(c) for the Full TTT reinforcement beams orientated along the x-direction (warp). As shown in Figure 10(a) and (c), up to point A the load-displacement response is linear elastic, with local increases in inter-ply shear strain. After the peak load at point B, delamination occurs around the neutral axis of the beam and TTT reinforcement, where shear strain is higher than at other locations. This delamination continues to point C, where the tows on the top of the beam begin to fracture under tensile stress.

At point D, the beam has begun to fail by fibre fracture on the top of the beam, with significant development of inter-laminar shear strains (see the peak shear strain locations in D

17

of Figure 10(c)). The large tensile crack propagates at and after the point of peak load, widening until ultimate catastrophic failure of the beam. Shown by a comparison between Figure 10(a) and (b), beams orientated along the x-direction (warp) are seen to have a more rapid drop off in load resisted, compared to the gradual load-bearing reduction of beams orientated along the y-direction (weft).

Figure 10(d) presents the finite element prediction of the short beam collapse event, as shown experimentally in Figure 10(c). The shear strain field γ_{xz} is shown. Up until point A, the prediction of the beam shows elastic deformation, which agrees well with experimental results. At Point B, a hinge forms in the FE predictions at the clamped end of the beam due to damage of the top warp tows and cohesive interaction. The shear strain field is shown to be almost identical to the shear strain field measured by DIC during experimental testing, i.e. Point B in Figure 10(c). The local strain is shown to be higher at the neutral axis and locations of TTT reinforcement. At point C, delamination has propagated longitudinally along the beam. However, the development of delamination is different from that observed in the experiment. During the experiment, the delamination propagates throughout the entire length of the beam, and this is not captured within the FE model. It is suggested this discrepancy is due to the use of an oversimplified constitutive model for the cohesive interaction, and lack of simulated confinement pressure from the TTT reinforcement and subsequent increase in frictional forces between composite layers. Finite element calculations also reveal the effect of TTT reinforcement on the load versus vertical roller deflection relation is small. The final image at point C of the FE prediction of the short beam collapse event along the warp direction without TTT reinforcement is presented in Figure 10(e). The prediction of the beam collapse with TTT reinforcement removed shows uninhibited delamination growth. However, this did not significantly affect the load-displacement

response. The numerically predicted delamination length for the Full TTT case was 3.0 mm; this corresponds well to the experimentally measured delamination length of 2.8 mm. The numerical prediction of the delamination length of the No TTT material was 5.5 mm. However, due to the reasons mentioned before, the model is not able to capture the secondary increase in load resisted.

In order to investigate the damage mechanisms throughout the beam thickness, Cross sectional X-Ray μCT scans of the beam post-testing are presented in Figure 11. Section a-a, a scan in between the binder position, demonstrates localised delamination, the length of which was bounded by the distance between TTT reinforcement tows. Section c-c, a scan also in between the binder position, did not demonstrate localised delamination, only tensile cracking. This highlights the heterogeneity and localisation of damage within the beam. At cross-sections located through the TTT reinforcement, for example scan b-b, no localised delamination was recorded. However, the tensile cracking was shown to be more pronounced at this location. These scans reveal localised, damage within the composite material. The short cantilever beam collapse response of a UD-laminate material is also presented in the supplementary data to this paper (Figure S.2). In short, delamination was recorded to propagate throughout the entire width of the UD-laminate composite beam, as opposed to the supressed, localised delamination of the 3D woven composite beams.

6. Concluding remarks

The collapse response of orthogonal 3D woven composites was investigated during in-plane tension and compression and out-of-plane bending load cases. The cantilever beam test has been shown to be effective in isolating the two collapse mechanisms of orthogonal 3D woven composite materials; bending dominated long beam tests, and shear dominated short beam tests.

The TTT reinforcement of 3D woven composites prevents delamination with long cantilever bending tests, and provides containment and limited changes to the post-peak load response with short beam tests. Localised delamination is shown in short cantilever beam tests, however, in long beam tests the failure mechanism is a large tensile crack and compressive buckling of longitudinal fibres at the clamped end. DIC analysis indicates increased local strain at TTT reinforcement positions for both long beam and short beam tests due to the presence of matrix pockets.

A finite element modelling strategy is presented and validated with experimental results of in-plane tension and compression test and cantilever bending tests. The FE method demonstrated excellent fidelity for in-plane uni-axial tension and compression tests. High levels of fidelity are also shown for the stiffness and peak load of long and short cantilever beam tests. However, the model is unable to capture the post initial peak load response of the short cantilever beam tests. Refinements to the cohesive interaction and damage evolution laws are suggested for advancements of the modelling strategy.

References

[1] Cox B, Dadkhah M, Morris W, Flintoff J. Failure mechanisms of 3D woven composites in tension, compression, and bending. Acta Metallurgica et Materialia. 1994;42:3967-84.

[2] Cristian I, Nauman S, Boussu F, Koncar V. A study of strength transfer from tow to textile composite using different reinforcement architectures. Applied Composite Materials. 2012;19:427-42.

[3] Callus P, Mouritz A, Bannister M, Leong K. Tensile properties and failure mechanisms of 3D woven GRP composites. Composites Part A: applied science and manufacturing. 1999;30:1277-87.

[4] Stig F, Hallström S. Assessment of the mechanical properties of a new 3D woven fibre composite material. Composites Science and Technology. 2009;69:1686-92.

[5] Cox BN, Dadkhah MS, Morris W. On the tensile failure of 3D woven composites. Composites Part A: applied science and manufacturing. 1996;27:447-58.

[6] Quinn J, McIlhagger A, McIlhagger R. Examination of the failure of 3D woven composites. Composites Part A: applied science and manufacturing. 2008;39:273-83.

[7] Leong K, Lee B, Herszberg I, Bannister M. The effect of binder path on the tensile properties and failure of multilayer woven CFRP composites. Composites Science and Technology. 2000;60:149-56.

[8] Bogdanovich AE. Advancements in manufacturing and applications of 3D woven preforms and composites. Proceeding of the 16th international conference on composites materials (ICCM-16)2007. p. 8-13.

[9] Cox B, Dadkhah M, Inman R, Morris W, Zupon J. Mechanisms of compressive failure in 3D composites. Acta Metallurgica et Materialia. 1992;40:3285-98.

[10] Budiansky B, Fleck NA. Compressive kinking of fiber composites: a topical review. Applied Mechanics Reviews. 1994;47:S246-S50.

[11] Guénon VA, Chou T-W, Gillespie Jr JW. Toughness properties of a three-dimensional carbon-epoxy composite. Journal of Materials Science. 1989;24:4168-75.

[12] Tanzawa Y, Watanabe N, Ishikawa T. Interlaminar fracture toughness of 3-D orthogonal interlocked fabric composites. Composites Science and Technology. 1999;59:1261-70.

[13] Pankow M, Salvi A, Waas A, Yen C, Ghiorse S. Resistance to delamination of 3D woven textile composites evaluated using End Notch Flexure (ENF) tests: Experimental results. Composites Part A: applied science and manufacturing. 2011;42:1463-76.

[14] Pankow M, Waas A, Yen C, Ghiorse S. Resistance to delamination of 3D woven textile composites evaluated using End Notch Flexure (ENF) tests: Cohesive zone based computational results. Composites Part A: applied science and manufacturing. 2011;42:1863-72.

[15] Fishpool D, Rezai A, Baker D, Ogin S, Smith P. Interlaminar toughness characterisation of 3D woven carbon fibre composites. Plastics, Rubber and Composites. 2013;42:108-14.

[16] Russell AJ, Street KN. Moisture and temperature effects on the mixed-mode delamination fracture of unidirectional graphite/epoxy. Delamination and debonding of materials, ASTM STP. 1985;876:349-70.

[17] Carlsson L, Gillespie J, Pipes R. On the analysis and design of the end notched flexure (ENF) specimen for mode II testing. Journal of composite materials. 1986;20:594-604.

[18] Martin R, Davidson B. Mode II fracture toughness evaluation using four point bend, end notched flexure test. Plastics, Rubber and Composites. 1999;28:401-6.

[19] Walter T, Subhash G, Sankar B, Yen C. Monotonic and cyclic short beam shear response of 3D woven composites. Composites Science and Technology. 2010;70:2190-7.

[20] Bosia F, Facchini M, Botsis J, Gmür T, de'Sena D. Through-the-thickness distribution of strains in laminated composite plates subjected to bending. Composites Science and Technology. 2004;64:71-82.

[21] Gerlach R, Siviour CR, Wiegand J, Petrinic N. In-plane and through-thickness properties, failure modes, damage and delamination in 3D woven carbon fibre composites subjected to impact loading. Composites Science and Technology. 2012;72:397-411.

[22] Yang B, Kozey V, Adanur S, Kumar S. Bending, compression, and shear behavior of woven glass fiber–epoxy composites. Composites Part B: Engineering. 2000;31:715-21.

[23] Hayat M, Suliman S. Mechanical and structural properties of glass reinforced phenolic laminates. Polymer testing. 1998;17:79-97.

[24] Cui W, Wisnom M, Jones M. Failure mechanisms in three and four point short beam bending tests of unidirectional glass/epoxy. The Journal of Strain Analysis for Engineering Design. 1992;27:235-43.

[25] Mujika F. On the difference between flexural moduli obtained by three-point and four-point bending tests. Polymer testing. 2006;25:214-20.

[26] Williams G, Trask R, Bond I. A self-healing carbon fibre reinforced polymer for aerospace applications. Composites Part A: applied science and manufacturing. 2007;38:1525-32.

[27] Khashaba U, Seif M. Effect of different loading conditions on the mechanical behavior of [0/±45/90] s woven composites. Composite Structures. 2006;74:440-8.

[28] Mallick PK. Fiber-reinforced composites: materials, manufacturing, and design: CRC press, 1993.

[29] Zhang D, Pankow M, Yen C, Ghiorse S, Waas A. Flexural Behavior of a Layer-to-Layer Orthogonal Interlocked Three-Dimensional Textile Composite. Journal of Engineering Materials and Technology. 2012;134:031009.

[30] Fukuda H. A new bending test method of advanced composites. Experimental Mechanics. 1989;29:330-5.

[31] Liu G, Thouless M, Deshpande V, Fleck N. Collapse of a composite beam made from ultra high molecular-weight polyethylene fibres. Journal of the Mechanics and Physics of Solids. 2014;63:320-35.

[32] Nagai K, Yokoyama A, Maekawa Z, Hamada H. Strength analysis for three-dimensional fibre reinforced composites. Adv Preform Mater. 1995:161-76.

[33] Quek SC, Waas AM, Shahwan K, Agaram V. Instabilities in braided textile composites under uniaxial compressive and biaxial loadings. 43 rd AIAA/ASME/ASCE/AHS/ASC Structures, Structural Dynamics, and Materials Conference, Denver, CO2002.

[34] Quek SC, Waas A, Shahwan KW, Agaram V. Compressive response and failure of braided textile composites: Part 2—computations. International Journal of Non-Linear Mechanics. 2004;39:649-63.

[35] Song S, Waas AM, Shahwan KW, Xiao X, Faruque O. Braided textile composites under compressive loads: modeling the response, strength and degradation. Composites Science and Technology. 2007;67:3059-70.

[36] Song S, Waas AM, Shahwan KW, Faruque O, Xiao X. Compression response of 2D braided textile composites: single cell and multiple cell micromechanics based strength predictions. Journal of composite materials. 2008.

[37] Huang H, Waas AM. Compressive response of Z-pinned woven glass fiber textile composite laminates: Modeling and computations. Composites Science and Technology. 2009;69:2338-44.

[38] Huang HJ, Waas AM. Modeling and predicting the compression strength limiting mechanisms in Z-pinned textile composites. Composites Part B: Engineering. 2009;40:530-9.

[39] Tan P, Tong L, Steven G. Behavior of 3D orthogonal woven CFRP composites. Part II. FEA and analytical modeling approaches. Composites Part A: applied science and manufacturing. 2000;31:273-81.

[40] Thuruthimattam B, Naik N. Mechanical characterization of hybrid 3D orthogonally woven composites. AIAA journal. 1998;98.

[41] Bogdanovich AE. Progressive failure modeling and strength predictions of 3-D woven composites. Proceedings of the 50th AIAA/ASME/ASCE/AHS/ASC Structures, Structural Dynamics, and Materials Conference, Palm Springs, CA, USA2009.

[42] Cox B, Carter W, Fleck N. A binary model of textile composites—I. Formulation. Acta Metallurgica et Materialia. 1994;42:3463-79.

[43] Xu J, Cox BN, McGlockton M, Carter W. A binary model of textile composites—II. The elastic regime. Acta Metallurgica et Materialia. 1995;43:3511-24.

[44] McGlockton M, Cox B, McMeeking R. A binary model of textile composites: III high failure strain and work of fracture in 3D weaves. Journal of the Mechanics and Physics of Solids. 2003;51:1573-600.

[45] Ansar M, Xinwei W, Chouwei Z. Modeling strategies of 3D woven composites: a review. Composite Structures. 2011;93:1947-63.

[46] Turner P, Liu T, Zeng X. Dynamic Response of Orthogonal Three-Dimensional Woven Carbon Composite Beams Under Soft Impact. Journal of applied mechanics. 2015;82:121008.

[47] ISO. 178: 2010. Plastics–Determination of flexural properties. International Standard Organization, Switzerland2010.

[48] EN. 63:1977 Methods of testing plastics. Glass reinforced plastics. Determination of flexural properties. Three point method. 1977.

[49] ASTM. D790-03. Standard Test Methods for Flexural Properties of Unreinforced and Reinforced Plastics and Electrical Insulating Materials2003. p. 1-11.

[50] Matzenmiller A, Lubliner J, Taylor R. A constitutive model for anisotropic damage in fiber-composites. Mechanics of materials. 1995;20:125-52.

[51] Hashin Z. Failure criteria for unidirectional fiber composites. Journal of applied mechanics. 1980;47:329-34.

[52] Soutis C, Fleck N, Smith P. Compression fatigue behaviour of notched carbon fibre-epoxy laminates. International journal of fatigue. 1991;13:303-12.

[53] Cui WC, Wisnom MR. Contact finite element analysis of three-and four-point short-beam bending of unidirectional composites. Composites Science and Technology. 1992;45:323-34.

Figure Captions

Figure 1. 3D orthogonal woven carbon composites showing Full through-the-thickness (TTT) reinforcement on the left and Half TTT reinforcement on the right, with the dimensions as the average measurements of the cured composites.

Figure 2. (a) Sketch of cantilever beam test, showing front surface painted for DIC analysis. (b) Sketch of composite beam oriented along the x-direction (warp). (For interpretation of the colour legend in this figure, the reader is referred to the web version of this article.)

Figure 3. Finite element model strategy employed within this study.

Figure 4. Typical stress-strain curves during quasi-static uni-axial material coupon tests of the full TTT 3D woven composites with longitudinal fibres oriented along the warp, weft and $\pm 45^{o}$ directions under (a) Tension; (b) Compression. Also presented is the FE predicted stress-strain response of the material. (For interpretation of the colour legend in this figure, the reader is referred to the web version of this article.)

Figure 5. Finite element simulation of uni-axial compression test along weft direction: (a) In-plane stress field σ_{yy} on the top surface layer immediately prior to sample failure (b) In-plane stress field σ_{yy} throughout the central weft tow stack immediately prior to fracture. The location of the central weft tow stack is shown in (a). (c) FE prediction of fracture surface with contour showing tow shear damage criterion, d_s, and (d) Photographic image of fracture surface from the compression experiment. (For interpretation of the colour legend in this figure, the reader is referred to the web version of this article.)

Figure 6. Finite element simulation of uni-axial tension test along weft direction. (a) In-plane stress field σ_{yy} on the top surface corresponding to peak load (b) FE prediction of fracture surface with contour showing shear damage d_s and (c) SEM image of fracture surface from the tension experiment. (For interpretation of the colour legend in this figure, the reader is referred to the web version of this article.)

Figure 7(a) Force applied by the roller against normalised roller deflection along the z-direction for a range of beam lengths. Beams oriented along the warp direction (Full TTT material). (b) The collapse load for a range of beam lengths orientated along the warp direction Full TTT. Also plotted are two predictions of collapse load values showing short beam shear dominated collapse and long beam bending dominated collapse regime.

Figure 8. Long (40 mm) cantilever beam tests results showing the force applied by the roller against vertical roller displacement relationship for beams oriented along (a) x-direction (warp); (b) y-direction (weft); (c) the progressive strain field with A, B, C and D corresponding to the respective points in (a) (obtained via DIC analysis), and the post-test

optical microscopic images showing localised damage of an edge weft tow and microbuckling of a warp tow constrained between the TTT reinforcement. (d) FE prediction of long beam (40mm) collapse. x-direction longitudinal strain field shown. (For interpretation of the colour legend in this figure, the reader is referred to the web version of this article.)

Figure 9(a) Micro-CT image post long beam collapse. Beam orientated along x-direction (warp) (b) location of CT image within the beam (at the location of TTT reinforcement). (For interpretation of the colour legend in this figure, the reader is referred to the web version of this article.)

Figure 10. Short (8 mm) cantilever beam test results. The force applied by the roller against vertical roller displacement relationship for beams orientated along (a) x-direction (warp); (b) y-direction (weft); (c) Progressive shear strain fields γ_{xz} with A, B, C and D corresponding to the load-displacement curve for the full TTT along the x-direction (warp) in (a). (d) Fe prediction of short beam collapse, showing shear strain γ_{xz}, points A, B and C correspond to the load-displacement curve for the Full TTT along the x-direction (warp) (e) Final montage of FE simulation of short beam with TTT reinforcement removed. Image corresponds to position C in (a). (For interpretation of the colour legend in this figure, the reader is referred to the web version of this article.)

Figure 11. μ-CT images of short beam post-collapse. Beam orientated along the x-direction (warp). (For interpretation of the colour legend in this figure, the reader is referred to the web version of this article.)
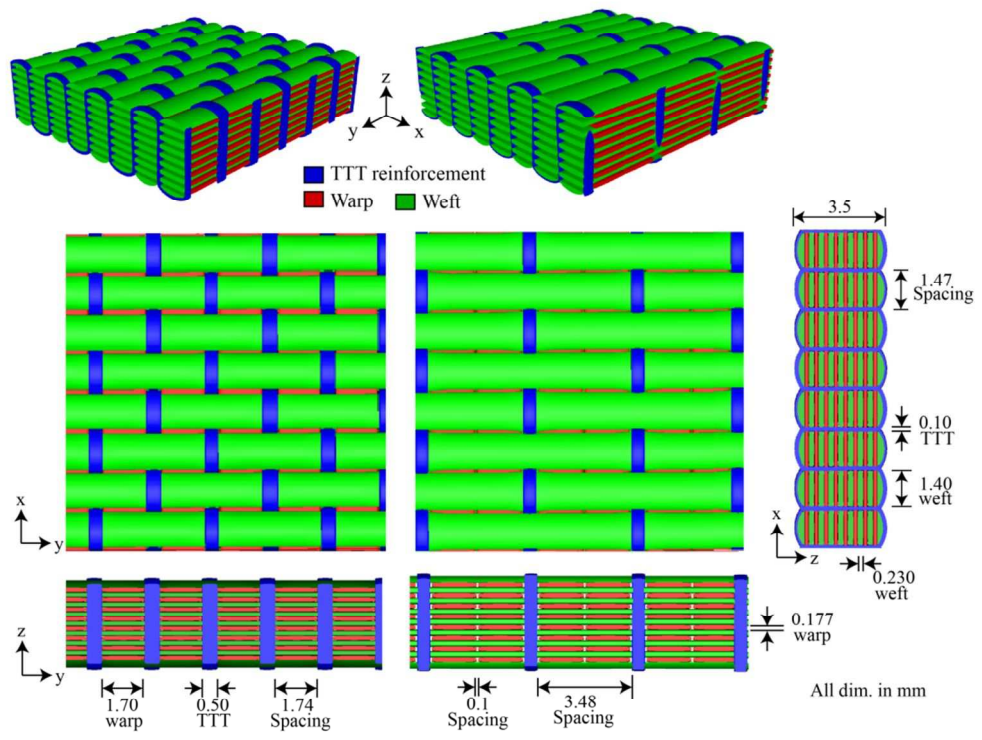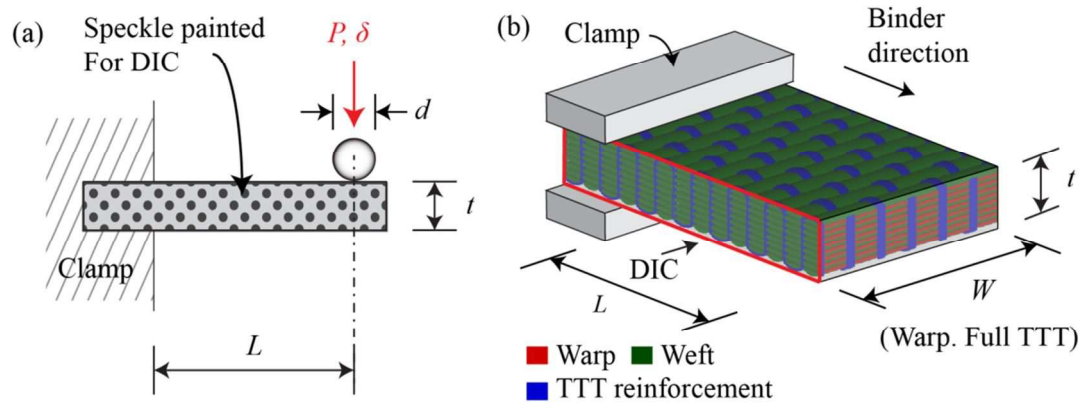
Figure 1

Figure 2
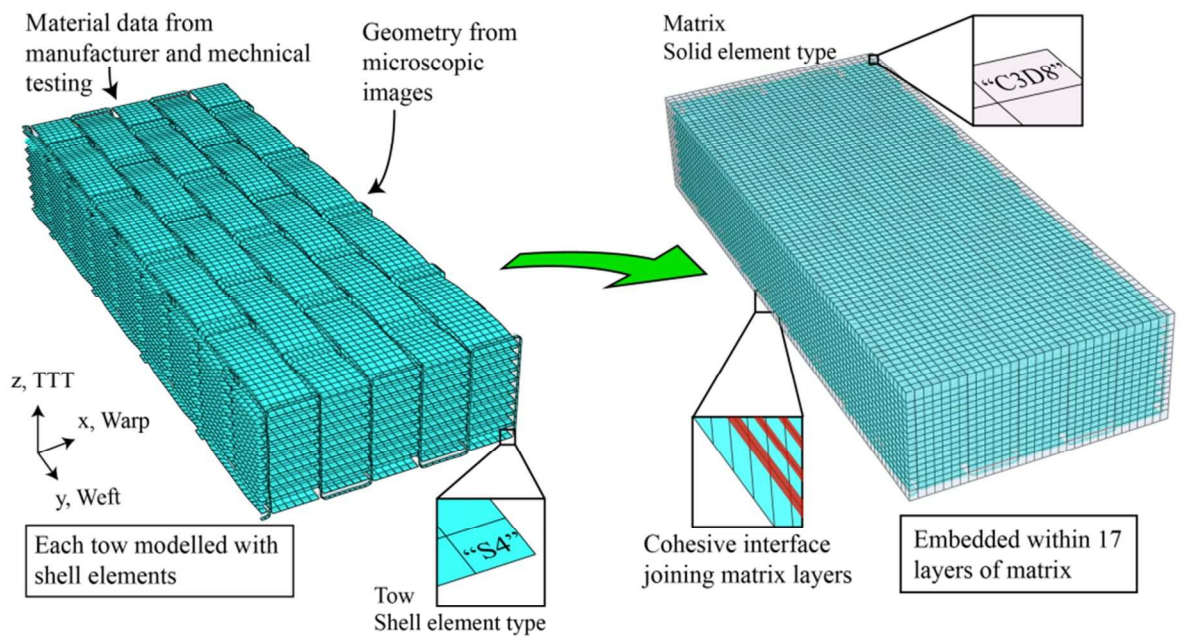
Figure 3

Figure 4

Figure 5

(a) Fracture surface location
Stress field prior to fracture on surface layer

a

Fixed end

a

TTT-reinforcement

Max stress = 1.72 GPa

Induced displacement

x

y, weft

1 mm

σ_yy GPa

0   0.425   0.85   1.275   1.7

(b)

z

x

y, weft

a

a

Shear damage, d_S

0   1

2 mm

(c)

1 mm

z

x, warp

Figure 6

(a) Warp. Full TTT

(b) Warp. Full TTT

$\tau_{xy} = 43$ MPa

Bending collapse

$$P_c^b = \frac{\sigma_x W t^2}{6L}$$

$$P_c^s = \tau_{xy} W t$$

Shear collapse

$\sigma_x = 590$ MPa

Figure 7

Figure 8

(a)

Clamp location

2 mm

2000 um

TTT

z

x

a   a

Slice 15.93 mm from O along y-axis

(b)

Location of CT image

a

a

z

O

y

x

15.93 mm

■ Warp ■ Weft ■ TTT reinforcement

Figure 9

35

(a)

(b)

(c) Full TTT Exp. warp direction

(d) Full TTT FE, warp direction

(e) No TTT FE, warp direction

Clamped end

Binder location

Tensile crack

Roller

Shear strain, γ_{XZ}

Binder location

Roller

Crack arrested by binder

Crack continues to propagate

Figure 10

36

Figure 11

Supplementary Data

Supplementary Data 1: UD-laminate cantilever beam experiments

UD laminate long (40mm) and short (8mm) cantilever beam bending results are now presented. The purpose of this testing is to provide an experimental comparison of the overall response with that of the 3D woven composite material. The material used is aerospace grade cross-ply carbon fibre with symmetrical 0/90° plies of 8 total layers giving a cured composite thickness of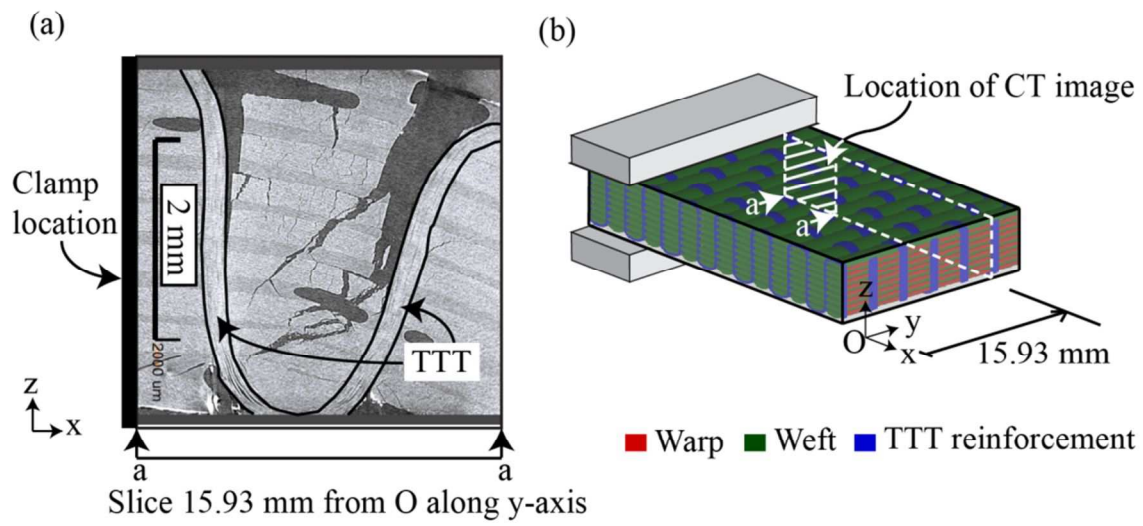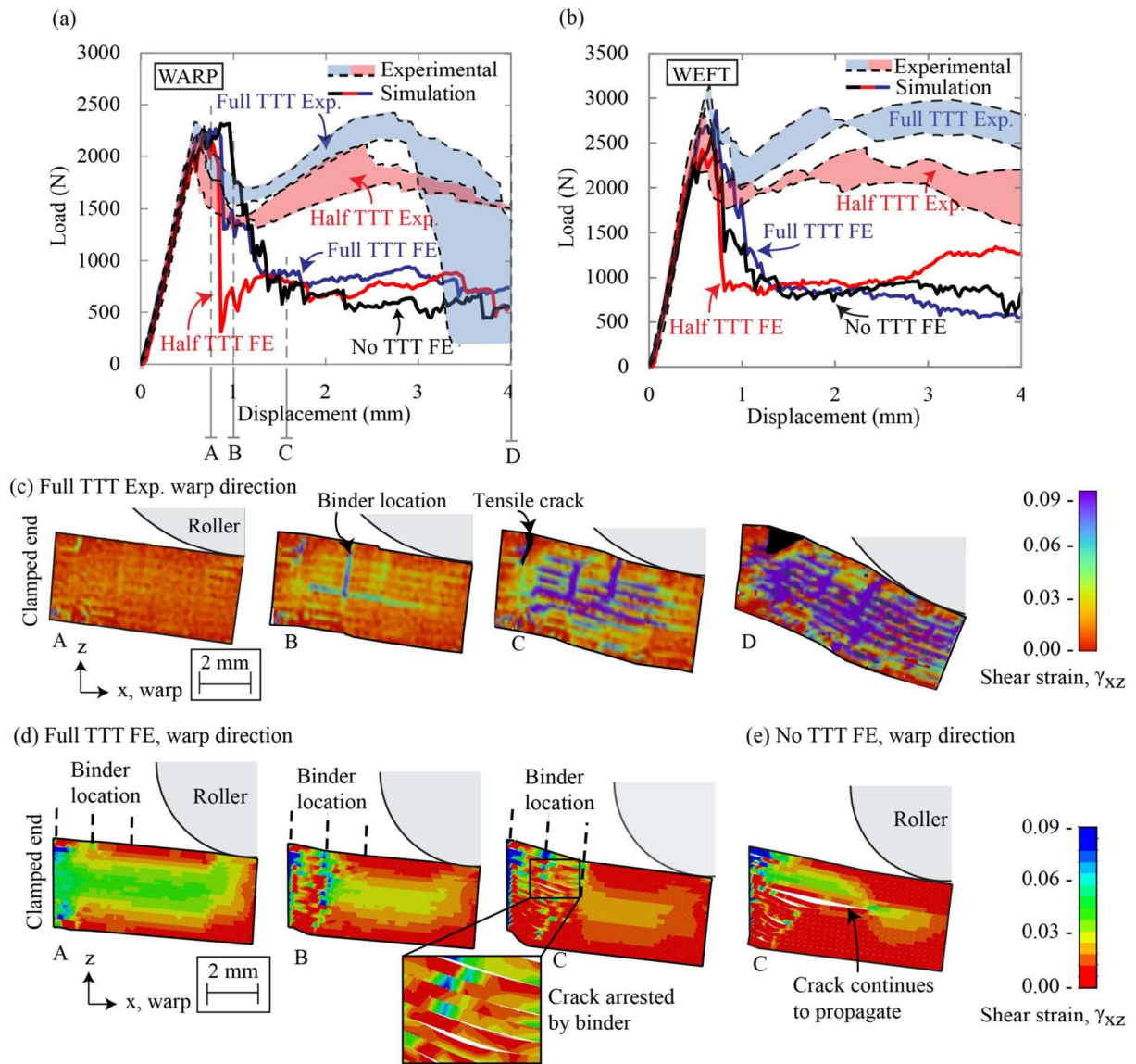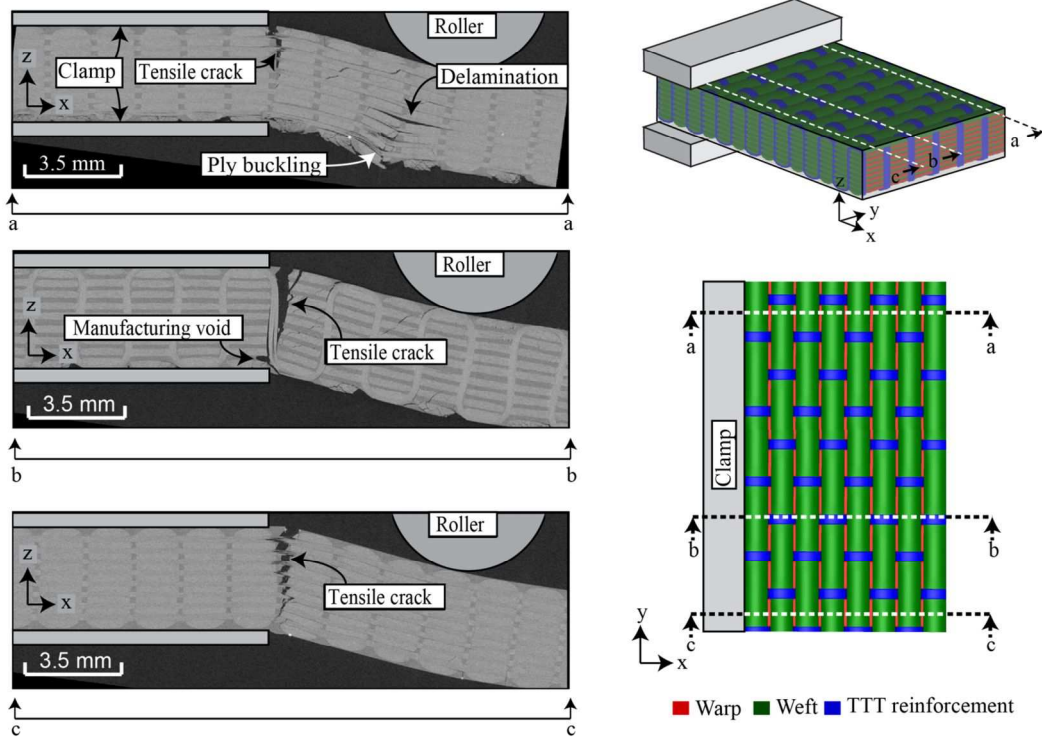 5.16mm. T700 (24k) fibres were used with a diameter of 7 μm. MTM57 epoxy matrix was used. Fibre volume fraction was 0.55. Due to differing geometry and material type a quantitative comparison cannot be made to the 3D woven material, only of the general collapse response.

UD laminate long beam

Figure S.1 presents the force applied by the roller against vertical roller displacement relationship for the long beam test. Linear deformation was demonstrated in the first phase up to point B. Past this linear stage, microbuckling occurs on the bottom compressive ply; this causes a reduction of stiffness. The resisted load increases until a peak load, at which wide-spread delamination occurs. This is different to the 3D woven material which retains full beam section and ultimate failure is tensile crack on the top surface. It should be noted that, unlike the results of the 3D woven material in warp direction, no tensile cracks are formed at the top surface. The failure mechanism becomes that of wide-spread delamination, and differs from tensile crack propagation presented by the 3D woven material in the main paper.

UD laminate short beam

As with the long beam UD laminate test, the short beam UD laminate canitlever beam test also experiences wide-spread delamination. Figure S.2(a) presents the force applied by the roller against

1

vertical deflection of the roller for the test, (b) presents a montage of deformation of the beam, and (c) presents optical microscopic images showing kink band formation on the bottom 0° ply. The first portion of the test, with point A in the middle, is in the linear elastic loading phase. Post peak-load, at point B, significant delamination has already occurred. From point B to point C there is seen to be a slight increase in the load resisted; this is because the delaminated plies are still resisting load. 45° intra-laminar shear matrix cracking within the transversely orientated plies is also shown from B onwards. Delamination and intra-laminar shear matrix cracking continue from point D onwards until ultimate loss of load bearing capability of the beam. Kinking bands are present in 0° plies below the neutral axis of the beam, and one is shown magnified in Figure S.2(b).

Numerical modelling constitutive model and material parameters

Description of the constitutive laws employed in the FE simulation

The constitutive model of Matzenmiller et al. [1] and Hashin [2] for fibre composites were employed to capture the observed collapse modes of tows and TTT-reinforcement. Both the weft and warp tows as well as TTT-reinforcement were modelled as shell elements embedded in matrix host elements. Note the local coordinate system for a tow is denoted by numbers, with 11 and 22 being longitudinal and transverse to fibre direction respectively. Each tow and TTT-reinforcement were treated as an orthotropic material under plane stress condition, i.e., $\sigma_{33} = \sigma_{13} = \sigma_{23} = 0$. The in-plane stress-strain relation for the materials without damage is given as;

$$\begin{Bmatrix} \varepsilon_{11} \\ \varepsilon_{22} \\ \gamma_{12} \end{Bmatrix} = \begin{bmatrix} 1/\overline{E}_{11} & -\overline{v}_{12}/\overline{E}_{11} & 0 \\ -\overline{v}_{21}/\overline{E}_{22} & 1/\overline{E}_{22} & 0 \\ 0 & 0 & 1/\overline{G}_{12} \end{bmatrix} \begin{Bmatrix} \sigma_{11} \\ \sigma_{22} \\ \sigma_{12} \end{Bmatrix} \tag{1}$$

Where σ_{ij} (i, j = 1,2) are in-plane stress components ; ε_{11} and ε_{22} are the direct strains in the x_1 and x_2 directions, respectively; γ_{12} is the engineering shear strain; $\overline{E}_{11}$, $\overline{E}_{22}$, $\overline{G}_{12}$, $\overline{v}_{12}$ and $\overline{v}_{21}$ are Young's modulus along the two directions , shear modulus and the two Poisson's ratios with

2

$\bar{v}_{21} = \left(\bar{E}_{22} / \bar{E}_{11} \right) \bar{v}_{12}$, respectively, which could be obtained via material tests. The undamaged

matrix material was treated as a linear elastic isotropic solid. The constitutive model is given as;

$$\begin{Bmatrix} \hat{\varepsilon}_{11} \\ \hat{\varepsilon}_{22} \\ \hat{\varepsilon}_{33} \\ \hat{\gamma}_{12} \\ \hat{\gamma}_{13} \\ \hat{\gamma}_{23} \end{Bmatrix} = \begin{Bmatrix} 1/E_m & -v/E_m & -v/E_m & 0 & 0 & 0 \\ -v/E_m & 1/E_m & -v/E_m & 0 & 0 & 0 \\ -v/E_m & -v/E_m & 1/E_m & 0 & 0 & 0 \\ 0 & 0 & 0 & 1/G_m & 0 & 0 \\ 0 & 0 & 0 & 0 & 1/G_m & 0 \\ 0 & 0 & 0 & 0 & 0 & 1/G_m \end{Bmatrix} \begin{Bmatrix} \hat{\sigma}_{11} \\ \hat{\sigma}_{22} \\ \hat{\sigma}_{33} \\ \hat{\sigma}_{12} \\ \hat{\sigma}_{13} \\ \hat{\sigma}_{23} \end{Bmatrix} \quad (2)$$

where $\hat{\sigma}_{ij}$ (i, j = 1,2,3) are stress components in the matrix; $\hat{\varepsilon}_{ii}$ (i = 1,2,3) are the direct strain

components and γ_{ij} (i, j = 1,2,3, i ≠ j) the shear strain components; E_m, G_m and v_m are Young's

modulus , shear modulus and Poisson's ratio, respectively, of the matrix material.

The damage model for weft and warp tows and TTT-reinforcement

For the tows and or TTT-reinforcement, the anisotropic damage model developed by Matzenmiller et

al. [1] as well as the damage initiation model for fibre reinforced composites developed by Hashin [2]

were employed in the simulation, which accounts for the four damage modes, i.e. fibre rupture under

tension, fibre buckling and kinking under compression, matrix cracking under transverse tension and

shear and matrix crushing under transverse compression or shearing. Similar to the concept of yield

surface in plasticity theory, the damage locus could be defined in the space of stress according to the

Hashin damage initiation criteria. For a stress state within the damage locus, the material is in

undamaged state and the stress-strain relation is described by Eq.(1). Damage initiates when the

critical stress state in the damage locus is attained or exceeded. Four scalar damage variables,

corresponding to the four damage modes, are introduced to represent the effects of the damage modes.

Post initiation of damage, the response of the material is governed by

$$\begin{Bmatrix} \varepsilon_{11} \\ \varepsilon_{22} \\ \gamma_{12} \end{Bmatrix} = \begin{Bmatrix} 1/[\overline{E}_{11}(1-d_f)] & -\overline{\nu}_{21}/[\overline{E}_{11}(1-d_f)] & 0 \\ -\overline{\nu}_{12}/[\overline{E}_{22}(1-d_m)] & 1/[\overline{E}_{22}(1-d_m)] & 0 \\ 0 & 0 & 1/[\overline{G}_{12}(1-d_s)] \end{Bmatrix} \begin{Bmatrix} \sigma_{11} \\ \sigma_{22} \\ \sigma_{12} \end{Bmatrix} \tag{3}$$

where
$$d_f = \begin{cases} d_f^t & \text{if } \sigma_{11} \geq 0 \\ d_f^c & \text{otherwise} \end{cases} \quad \text{and} \quad d_m = \begin{cases} d_m^t & \text{if } \sigma_{22} \geq 0 \\ d_m^c & \text{otherwise} \end{cases} \tag{4}$$

Here, d_f^t, d_f^c, d_m^t and d_m^c are the damage variables for fibre damage under tension and compression,

matrix damage under tension and compression, respectively. d_s is the shear damage variable,

defined as

$$d_s \equiv 1 - (1 - d_f^t)(1 - d_f^c)(1 - d_m^t)(1 - d_m^c) \tag{5}$$

The shear damage variable is presented in the main text of this paper in order to visualise the location

of predicted damage during finite element simulations of in-plane uni-axial coupon tests. It is useful

as a "resultant" damage variable; combining tension and compression for both longitudinal and

transverse directions.

In the undamaged state, the damage variables are set to zeros. During the stage of damage initiation

and evolution, damage variables evolve from zeros to a maximum value of unity controlled by the

strain in the material. The damage evolution law follows that proposed by Matzenmiller et al. [1]. The

damage will only develop when the stress state exceeds the critical stress surface given by

$$\frac{\langle \sigma_{11} \rangle}{(1 - d_f^t)\overline{X}^T} \leq 1 \tag{6}$$

$$\frac{-\langle \sigma_{11} \rangle}{(1 - d_f^c)\overline{X}^C} \leq 1 \tag{7}$$

$$\left(\frac{\langle \sigma_{11} \rangle}{(1 - d_m^t)\overline{Y}} \right)^2 + \left(\frac{2\sigma_{12}}{(1 - d_s)\overline{Y}} \right)^2 \leq 1 \tag{8}$$

4

or

$$\left(\frac{\langle -\sigma_{22}\rangle}{(1-d_m^c)\overline{Y}}\right)^2+\left(\frac{2\sigma_{12}}{(1-d_s)\overline{Y}}\right)^2\leq 1 \qquad (9)$$

where $\langle \; \rangle$ represents the Macaulay bracket of value zero when its augment is negative. $\overline{X}^T$ and $\overline{X}^C$ denote the tensile and compressive strength at damage initiation during loading along the fibre direction. $\overline{Y}$ denotes the tensile and compressive strength along the transverse direction.

The four independent damage variables, d_f^t, d_f^c, d_m^t and d_m^c, increase if the stress state lies beyond the critical space defined in Eqs. (6) to (9). The damage variables are assumed to evolve in a way that the stress decreases linearly with increasing strain once damage initiates. The following relations are used to update the damage variables;

$$d_f^t = \frac{\dfrac{2J_f^t}{l_e\overline{X}^T}\left(\langle \varepsilon_{11}\rangle - \overline{X}^T/\overline{E}_{11}\right)}{\langle \varepsilon_{11}\rangle\left(\dfrac{2J_f^t}{l_e\overline{X}^T}-\overline{X}^T/\overline{E}_{11}\right)}\leq 1 \qquad (10)$$

$$d_f^c = \frac{\dfrac{2J_f^c}{l_e\overline{X}^c}\left(\langle \varepsilon_{11}\rangle - \overline{X}^c/\overline{E}_{11}\right)}{\langle \varepsilon_{11}\rangle\left(\dfrac{2J_f^c}{l_e\overline{X}^c}-\overline{X}^c/\overline{E}_{11}\right)}\leq 1 \qquad (11)$$

$$d_m^t = \frac{\dfrac{2J_m}{l_e\overline{Y}}\left(\sqrt{\langle \varepsilon_{22}\rangle^2 + \varepsilon_{12}^2}-\overline{Y}/\overline{E}_{22}\right)}{\sqrt{\langle \varepsilon_{22}\rangle^2 + \varepsilon_{12}^2}\left(\dfrac{2J_m}{l_e\overline{Y}}-\overline{Y}/\overline{E}_{22}\right)}\leq 1 \qquad (12)$$

5

$$d_m^c = \frac{\frac{2J_m}{l_e \overline{Y}}\left(\sqrt{\langle -\varepsilon_{22} \rangle^2 + \varepsilon_{12}^2} - \overline{Y}/\overline{E}_{22}\right)}{\sqrt{\langle -\varepsilon_{22} \rangle^2 + \varepsilon_{12}^2}\left(\frac{2J_m}{l_e \overline{Y}} - \overline{Y}/\overline{E}_{22}\right)} \leq 1 \tag{13}$$

where l_e is a characteristic length scale which is same to the length across a finite element; J_f^t, J_f^c and J_m are the tensile fibre fracture energy, compressive fibre fracture energy and the matrix fracture energy, respectively.

The damage model for the matrix material

The matrix material was treated as a J2-flow theory based elastic-ideally plastic solid with the undamaged elastic response dictated by Eqn. (2) and uniaxial tensile strength $\overline{\sigma}_Y^o$. In order to model the damage in matrix, the damage initiation criteria was defined as $\overline{\varepsilon}_{pl} = \overline{\varepsilon}_c$, where $\overline{\varepsilon}_{pl}$ and $\overline{\varepsilon}_c$ denote the von Mises effective plastic strain and a critical strain , respectively . After damage initiation, a damage variable, D $(0 \leq D \leq 1)$, is employed for degradation of the elasticity, i.e. $(1-D)E_m$, and softening of the yield stress, i.e $(1-D)\hat{\sigma}_Y^o$, which is dictated by the following equation;

$$\frac{dD}{dt} = \frac{L_e \hat{\sigma}_Y^o}{2J_m}\frac{d\overline{\varepsilon}_{pl}}{dt} \tag{14}$$

where L_e denotes a characteristic length scale , J_m the fracture energy and t time .The damage variable is set to zero before damage initiation . The constitutive model employed for matrix material does not account for volume changes. More elaborate analysis could be found in Ref [3]. In the current study, omitting the effect has negligible influence on the numerical predictions as the behaviour of the coupons and cantilever beams is dominated either by the in-plane tows or the interlaminar properties.

6

Cohesive law for the interface between tows through thickness

The matrix material was split into 17 layers through the thickness, corresponding to the 9 weft and 8 warp tow layers. A cohesive contact law was used to model the interface between layers, which simulates the traction-separation behaviour between them and allows the FE model to simulate delamination at these locations. It is noted that it was at these locations that delamination occurred during experimental testing. For an undamaged cohesive contact, the behaviour across the interface is dictated by the following elastic response

$$
\begin{Bmatrix} t_n \\ t_s \\ t_t \end{Bmatrix} = \begin{Bmatrix} k_n & 0 & 0 \\ 0 & k_s & 0 \\ 0 & 0 & k_t \end{Bmatrix} \begin{Bmatrix} \delta_n \\ \delta_s \\ \delta_t \end{Bmatrix}
\tag{15}
$$

where t_n, δ_n and k_n denote the normal traction, separations and stiffness, respectively; $\{t_s, t_t\}$, $\{\delta_s, \delta_t\}$ and $\{k_s, k_t\}$ the two shear tractions, separations and coefficients of stiffness , respectively. The behaviour is uncoupled, i.e. pure normal separation in isolation does not cause any cohesive forces in any of the shear directions and pure shear displacement does not cause any normal cohesive forces.

The failure mechanism of the cohesive contact consists of both a damage initiation criterion and a damage evolution law. Damage develops when the traction stresses lies outside the following surface;

$$
\left[\frac{\langle t_n \rangle}{(1-\hbar)T_n} \right]^2 + \left[\frac{\langle t_s \rangle}{(1-\hbar)T_s} \right]^2 + \left[\frac{\langle t_t \rangle}{(1-\hbar)T_s} \right]^2 \leq 1
\tag{16}
$$

where T_n and T_s denote the maximum allowable uncoupled traction forces along normal and shear directions, respectively; $\hbar\left(0 \leq \hbar \leq 1\right)$ denotes the damage variable for cohesive contact with $\hbar = 0$

7

for undamaged state and $\hbar = 1$ for fully damaged state. The damage variable is defined in terms of the fracture energy, J_G, given as

$$\hbar = \frac{\dfrac{2J_G}{t_e^0}\left(\delta_e^{max} - \delta_e^0\right)}{\delta_e^{max}\left(\dfrac{2J_G}{t_e^0} - \delta_e^0\right)} \leq 1 \tag{17}$$

where δ_e^{max} is the maximum value of the effective separation that occurs during loading; t_e^0 and δ_e^0 are the effective traction and separation at the damage initiation point. The effective separation, δ_e, and effective traction, t_e, is given by the following relationship from Camanho and Dávila [4]

$$\delta_e \equiv \sqrt{\langle\delta_n\rangle^2 + \delta_s^2 + \delta_t^2} \tag{18}$$

$$t_e \equiv \sqrt{\langle t_n\rangle^2 + t_s^2 + t_t^2} \tag{19}$$

The damage evolution is defined as linear softening and, at any given moment, has the form

$$t_n = \begin{cases} (1-\hbar)k_n\delta_n & \text{when } \delta_n > 0 \\ k_n\delta_n & \text{otherwise} \end{cases} \tag{20}$$

$$t_s = (1-\hbar)k_s\delta_s \tag{21}$$

$$t_t = (1-\hbar)k_t\delta_t \tag{22}$$

Note that in compression, i.e. when $\delta_n \leq 0$, the interaction between the two matrix layers is reduced to a penalty contact algorithm. In order to simulate the interaction behaviour of fully damaged cohesive contacts the "general contact" option within ABAQUS was used with a tangential friction coefficient of 0.3.

The normal and shear stiffness, k_n and k_s respectively, were estimated from manufacturers data. An initial interface length of 0.1 mm was assumed. The normal and shear traction, t_n and t_s respectively, were estimated from the peak stress during the matrix dominated ±45° material tensile test results. The fracture energy, J_G, was not directly measured and estimated from ±45° material tensile test results. The values of these parameters are given in Table 1.

Calibration of material properties employed in FE simulations

Weft tows, warp tows and TTT-reinforcement as shell elements

Ten parameters are required in order to define the elastic property , damage initiation and damage evolution of tows and TTT-reinforcement, i.e. $\overline{E}_1, \overline{E}_2, \overline{\nu}_{12}, \overline{G}_{12}, \overline{X}^T, \overline{X}^C, \overline{Y}, \overline{J}_1^T, \overline{J}_1^C$ and J_m. These parameters could be estimated using the rule of mixture based on either manufacturer's data or material coupon tests. We first consider application of manufacturer's data. Consider a tow with fibre volume fraction V_t, we have;

$$\overline{E}_1 = V_t E_f + (1 - V_t) E_m \tag{23}$$

$$\overline{G}_{12} = \frac{G_{12f} G_m}{V_t G_m + (1 - V_t) G_{12f}} \tag{24}$$

$$\overline{\nu}_{12} = V_t \nu_f + (1 - V_t) \nu_m \tag{25}$$

$$\overline{X}^T = V_t X_f + (1 - V_t) \overline{\sigma}_Y^o \tag{26}$$

$$\overline{X}^C = V_t X_f + (1 - V_t) \overline{\sigma}_Y^o \tag{27}$$

9

where the A-38 carbon fibres of diameter 7 μm within the fibre reinforcement were assumed to be isotropic and using ISO 10618 test methods have a tensile modulus E_f of 240 GPa, and a longitudinal tensile strength X_f of 3800 MPa. Fibre Poisson's ratio ν_f was assumed to be 0.25 giving an in-plane shear modulus G_{12f} of 96 GPa. The transverse longitudinal modulus, $\overline{E}_2$, is matrix dominated and can simply be estimated as the Young's modulus of cured epoxy matrix 3.5 GPa. Warp and weft tows contained 6000 fibres, and TTT reinforcement tows contained 3000 fibres. The fibre volume fractions of warp, weft and TTT reinforcement tows were measured using microscopic cross sectional images as 0.785, 0.692, and 0.795, respectively.

Alternatively, these parameters could be estimated based on experimental measurement as follows. Let V_{tow}^{weft} and V_{tow}^{warp} denote the volume fractions of weft tows and warp tows within a composite test sample, respectively, which can be calculated as,

$$V_{tow}^{weft} = \frac{n_{weft} A_{tow}^{weft}}{A_y}, \quad V_{tow}^{warp} = \frac{n_{warp} A_{tow}^{warp}}{A_x} \tag{28}$$

where A_{tow}^{wef} and A_{tow}^{warp} denote the average transverse cross section areas for a weft tow and a warp tow, respectively, n_{weft} and n_{warp} the numbers of the weft tows and warp tows in the composite sample and A_y and A_x are the areas of cross sections of the composite along the y (weft) and x (warp) axis, respectively. Based on the rule of mixtures we have

$$\overline{E}_1 = \frac{E_x^T - (1 - V_{tow}^{warp})E_m}{V_{tow}^{warp}}, \overline{G}_{12} = \frac{G_{xy}G_m V_{tow}^{warp}}{V_{tow}^{arp}G_m + (1 - V_{tow}^{warp})G_{xy}}, \overline{\nu}_{12} = \frac{\nu_{xy} - (1 - V_{tow}^{warp})\nu_m}{V_{tow}^{warp}} \tag{29}$$

$$\overline{X}^T = \left(\frac{E_x^T - (1 - V_{tow}^{warp})E_m}{V_{tow}^{warp}} \right) \frac{X_x^T}{E_x^T}, \overline{X}^C = \left(\frac{E_x^C - (1 - V_{tow}^{warp})E_m}{V_{tow}^{warp}} \right) \frac{X_x^C}{E_x^C} \tag{30}$$

for warp tows, and

10

$$\overline{E}_1^T = \frac{E_y^T - (1 - V_{tow}^{warp})E_m}{V_{tow}^{warp}}, \overline{G}_{12} = \frac{G_{xy}G_m V_{tow}^{weft}}{V_{tow}^{weft}G_m + (1 - V_{tow}^{weft})G_{xy}}, \overline{v}_{12} = \frac{v_{xy} - (1 - V_{tow}^{weft})v_m}{V_{tow}^{weft}} \qquad (31)$$

$$\overline{X}^T = \left(\frac{E_y^T - (1 - V_{tow}^{weft})E_m}{V_{tow}^{weft}}\right)\frac{X_y^T}{E_y^T}, \overline{X}^C = \left(\frac{E_y^T - (1 - V_{tow}^{weft})E_m}{V_{tow}^{weft}}\right)\frac{X_y^C}{E_y^C} \qquad (32)$$

for weft tows. Here, $\{E_x^T, E_x^C, X_x^T, X_x^C\}$ and $\{E_y^T, E_y^C, X_y^T, X_y^C\}$ are the measured material tensile

Young's modulus, compressive Young's modulus, tensile strength and compressive strength along x

(warp) direction and y (weft) direction, respectively, v_{xy} is the measured in-plane Poisson's ratio.

These parameters are obtained by the 0/90° coupon tests, as the failure of the 0/90° test coupons was

governed by the failure of the warp/weft tows. It is assumed in Eqns. (30) and (32), that the strain to

failure of the tows along the loading direction within a test sample is identical to that of the composite

itself. G_{xy} is the measured shear modulus obtained by the ±45° coupon tests.

The material parameters estimated based on manufacturer's data and material coupon tests are

compared in Table 2. These material data were employed in FE simulation of 0/90° coupon tests in

comparison with experimental measurement. It was demonstrated that the application of the rule of

mixtures to manufacturer's data of the fibres and matrix, described in Eqns. (23) through (27),

overestimated $\overline{E}_1$, $\overline{X}^T$ and $\overline{X}^C$. This is commonly attributed to (i) inherent fibre waviness within

the composite, which reduces the stiffness, (ii) fibre misalignment and micromechanical flaws within

the composite, which reduces tensile strength, and (iii) kink band formation and microbuckling of

fibres, which reduces the compressive strength of tows [5]. However, the values for tow shear

modulus, $\overline{G}_{12}$, obtained in Equations (29) and (31) are lower than that of pure matrix material, which

are unrealistic. Thus, Eqn. (24) using manufacturer's data was used to calculate tow shear modulus.

The tow transverse modulus, $\overline{E}_2$, is dominated by matrix. Again, this value was taken from

manufacturer's data. There is a doubling up of the elastic properties in the transverse direction as the

11

same volume is occupied by both the matrix and the tow. A parametric study was conducted for both in-plane and cantilever beam bending simulations and revealed that even if the transverse stiffness of the tows were reduced by ten times, in order to avoid superposition, there was no effect on the results. It can be concluded that the model is insensitive to matrix superposition effects. The transverse strength of tows, $\overline{Y}$, is matrix dominated. The value for the transverse strength of tows was estimated from the onset of non-linearity from the tensile material coupon tests with fibres orientated at ±45 from the loading axis, i.e. $\overline{Y} = 80\ \text{MPa}$.

The longitudinal tensile and compressive tow fracture energies, $\overline{J}_1^t$ and $\overline{J}_1^c$ were calculated using the following equations;

$$\overline{J}_1^t = 0.5 \times \frac{l_e \left(\overline{X}_1^T\right)^2}{\overline{E}_1} \times 1.2 \tag{33}$$

and

$$\overline{J}_1^c = 0.5 \times \frac{l_e \left(\overline{X}_1^C\right)^2}{\overline{E}_1} \times 1.2 \tag{34}$$

The transverse fracture energy of the tow is assumed to be the same as the matrix material, again taken from ±45º coupon tests. The fibre volume fraction of the TTT reinforcement was calculated as being 0.795, almost identical to that of the warp tows. To avoid any material testing along the TTT reinforcement direction, the warp and TTT reinforcement material properties were assumed to be the same within the model.

Matrix material as solid elements

The Young's modulus, E_m, and density, ρ_m, employed in the FE simulation for the pure matrix material, i.e. Prime 20LV epoxy matrix, were taken from data provided by the manufacturer, i.e.

12

$E_m = 3.5\,\text{GPa}$ and $\hat{\rho} = 1.144\,\text{g/cm}^3$. The yield strength, $\hat{\sigma}_Y^o$, fracture strain , $\hat{\varepsilon}_c$, and fracture energy, J_m, were estimated from ±45º tensile coupon tests , in which the failure of test samples is dominated by the strength of the matrix material, i.e. $\hat{\sigma}_Y^o = 80\,\text{MPa}$, $\hat{\varepsilon}_c = 0.25$ and $J_m = 650\,\text{Jm}^{-2}$. The Poisson's ratio ν_m was estimated as 0.3. Table 3 presents the material properties for the reinforcement tows and the matrix material within the FE model.

Figure Captions

Figure S.1. Long (40mm) cantilever beam test of a UD laminate material. (a) force applied by the roller against vertical roller displacement relationship (b) photographic montage during the test. The surface of the beam is speckle painted to allow for easy tracking.

Figure S.2. Short (8mm) beam cantilever beam test of UD laminate material. (a) force applied by the roller against vertical roller displacement relationship (b) montage of deformation throughout the test showing delamination and intra-laminar matrix cracking (c) optical microscopic images of the bottom ply.

Table captions

Table 1. Material parameters for the cohesive contact between matrix slices

Table 2. Tow material properties calculated from manufacturer's data and material testing. The values underlined give the best fit between FE simulation results and experimental measurement.

Table 3. Material properties of matrix and tows for the composite material used in the constitutive model in the FE calculations.

References

1. Matzenmiller, A., J. Lubliner, and R. Taylor, A constitutive model for anisotropic damage in fiber-composites. Mechanics of materials, 1995. **20**(2): p. 125-152.
2. Hashin, Z., Failure criteria for unidirectional fiber composites. Journal of applied mechanics, 1980. **47**(2): p. 329-334.
3. Rabinowitz.S, I.M. Ward, and J.S.C. Parry, The effect of hydrostatic pressure on the shear yield behaviour of polymers. Journal Material Science 1970. **5**: p. 29-39.
4. Camanho, P.P. and C.G. Dávila, Mixed-mode decohesion finite elements for the simulation of delamination in composite materials. NASA-Technical paper, 2002. **211737**(1): p. 33.
5. Cox, B., et al., Mechanisms of compressive failure in 3D composites. Acta Metallurgica et Materialia, 1992. **40**(12): p. 3285-3298.

14

Figure S.1

15

(a)

(b)

Delamination

(c)
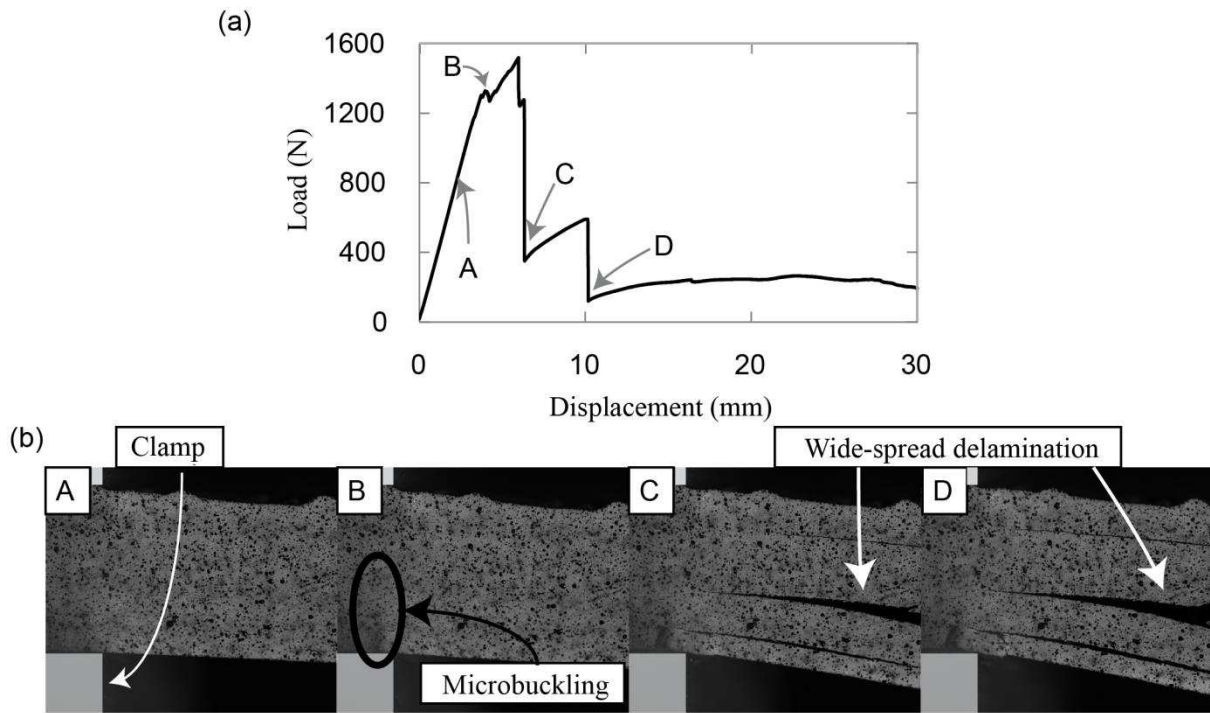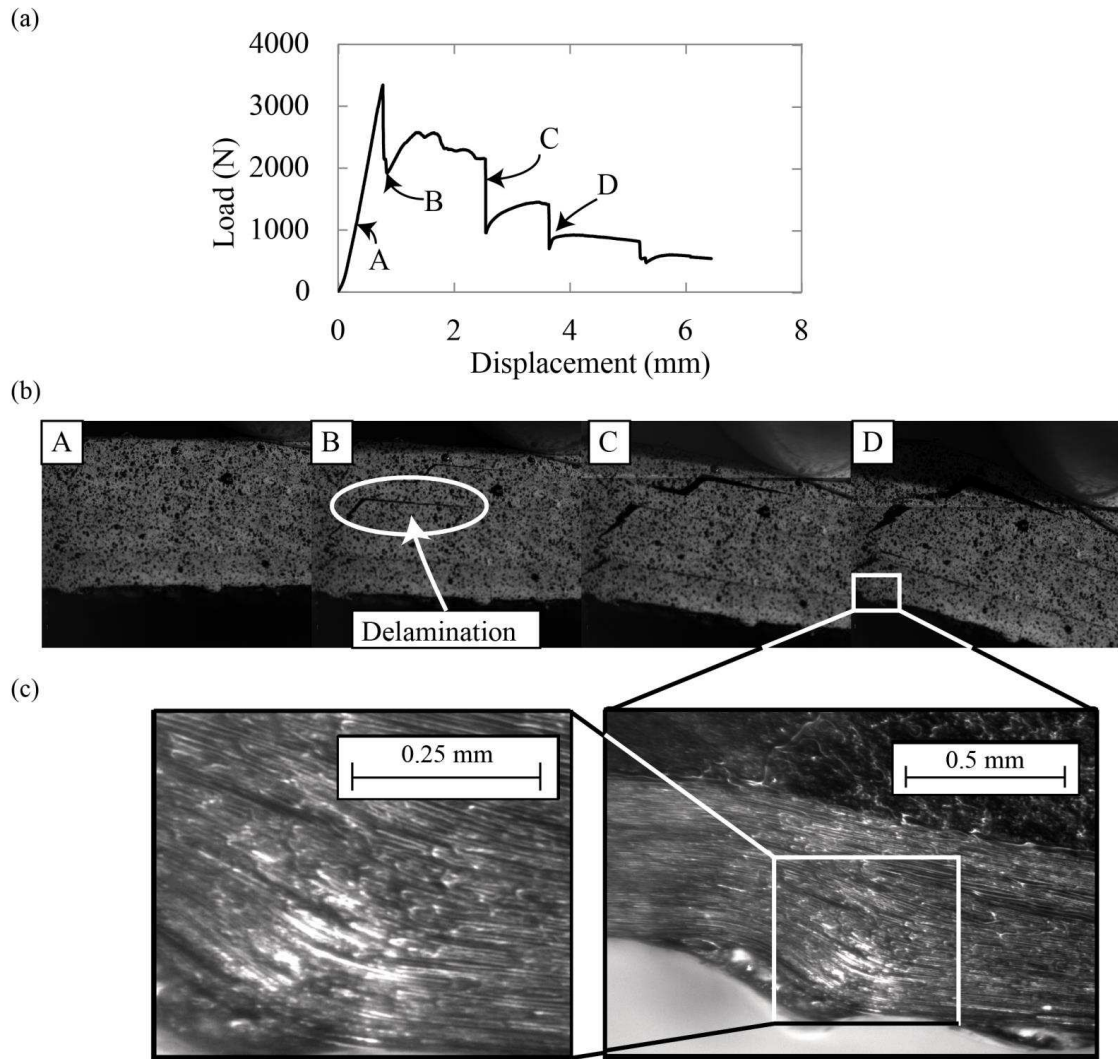
Figure S.2

Table 2

Property	Value
Normal stiffness, k_n	35 GPa mm^{-1}
Shear stiffness, k_s, k_t	20 GPa mm^{-1}
Normal traction, t_n	80 MPa
Shear traction, t_s, t_t	40 MPa
Fracture energy, J_G	650 J m^{-2}

Table 2

Property	Calculations from Manufacturer's data (Equations 25-29)	Calculations from Material tests (Equations 31-32)
Warp		
$\overline{E}_1$ (GPa)	189.2	<u>146.8</u>
$\overline{E}_2$ (GPa)	<u>3.5</u>	N/A
$\overline{v}_{12}$	0.26	<u>0.35</u>
$\overline{G}_{12}$ (GPa)	<u>14.37</u>	0.46
$\overline{X}^T$ (GPa)	3.15	<u>2.02</u>
$\overline{X}^C$ (GPa)	3.15	<u>1.61</u>
$\overline{Y}$ (MPa)	83	<u>80</u>
Weft		
$\overline{E}_1$ (GPa)	167.3	<u>137.4</u>
$\overline{E}_2$ (GPa)	<u>3.5</u>	N/A
$\overline{v}_{12}$	0.27	<u>0.35</u>
$\overline{G}_{12}$ (GPa)	<u>7.16</u>	1.06
$\overline{X}^T$ (GPa)	2.86	<u>1.72</u>
$\overline{X}^C$ (GPa)	2.86	<u>1.10</u>
$\overline{Y}$ (MPa)	83	<u>80</u>

Table 3

Material	Property	Value
Matrix	E_m (GPa)	3.5
	ν_m	0.3
	Density (g mm^{-3})	0.001144
	Yield Stress σ_y (MPa)	80
	Fracture strain ε_f	0.25
	J_m (Jm^{-2})	650
Warp Yarn/TTT reinforcement	$\overline{E}_1$ (GPa)	146.8
	$\overline{E}_2$ (GPa)	3.5
	$\overline{\nu}_{12}$	0.25
	$\overline{G}_{12}, \overline{G}_{13}, \overline{G}_{23}$ (GPa)	14.37
	Density (g mm^{-3})	0.001628
	$\overline{X}^T$ (MPa)	2020
	$\overline{X}^C$ (MPa)	1610
	$\overline{Y}$ (MPa)	80
	$\overline{X}^s, \overline{Y}^s$ (MPa)	40
	$\overline{J}_1^t/l_e$ (MPa)	16.68
	$\overline{J}_1^c/l_e$ (MPa)	10.6
	J_m/l_e (MPa)	7.9
Weft Yarn	$\overline{E}_1$ (GPa)	135.7
	$\overline{E}_2$ (GPa)	3.5
	$\overline{\nu}_{12}$	0.25
	$\overline{G}_{12}, \overline{G}_{13}, \overline{G}_{23}$ (GPa)	7.16
	Density (g mm^{-3})	0.00157
	$\overline{X}^T$ (MPa)	1720
	$\overline{X}^C$ (MPa)	1110
	$\overline{Y}$ (MPa)	80
	$\overline{X}^s, \overline{Y}^s$ (MPa)	40
	$\overline{J}_1^t/l_e$ (MPa)	13.08
	$\overline{J}_1^c/l_e$ (MPa)	5.45
	J_m/l_e (MPa)	7.90